3D Image Reconstruction from Compton camera data

Peter Kuchment[*]and Fatma Terzioglu[†]

Abstract

In this paper, we address analytically and numerically the inversion of the integral transform (*cone* or *Compton* transform) that maps a function on $\mathbb{R}^3$ to its integrals over conical surfaces. It arises in a variety of imaging techniques, e.g. in astronomy, optical imaging, and homeland security imaging, especially when the so called Compton cameras are involved.

Several inversion formulas are developed and implemented numerically in $3D$ (the much simpler $2D$ case was considered in a previous publication).

Introduction

In this paper, we address analytic and numerical aspects of inversion of the integral transform that maps a function on $\mathbb{R}^n$ to its integral over conical surfaces (with main concentration on the $3D$ case, while the much simpler $2D$ case was treated in [37]). It arises in a variety of imaging techniques, e.g. in optical imaging [12], but most prominently when the so called *Compton cameras* are used, e.g. in astronomy, SPECT medical imaging [11,33], as well as in homeland security imaging [1,2,19,39]. We will call it *cone* or *Compton* transform (in 2D, the names *V-line transform* and *broken ray transform* are also used),

---

[*]Department of Mathematics, Texas A&M University, College Station, TX 77843-3368, USA, e-mail: kuchment@math.tamu.edu

[†]Same department, e-mail: fatma@math.tamu.edu

Being already used in astronomy, the application of Compton cameras in nuclear medicine was first proposed in [11] as an alternative to gamma (or Anger) cameras used in medical SPECT (Single Photon Emission Tomography) imaging. The drawback of conventional gamma cameras is that they utilize mechanical collimation in order to determine the direction of an incoming gamma photon. The signal acquired by a gamma camera is weak because only the γ-rays approaching the detector in a very small angle of directions (see Fig. 1(a)) can pass through the collimator [6]. In addition, the camera must be rotated to obtain projections from different directions.

On the other hand, Compton cameras make use of the Compton scattering effect (see Fig. 1(b)) to locate the radioactive source. The absence of mechanical collimation resolves the issue of low efficiency and the need for rotating the camera. It also facilitates the design of hand-held devices [23].
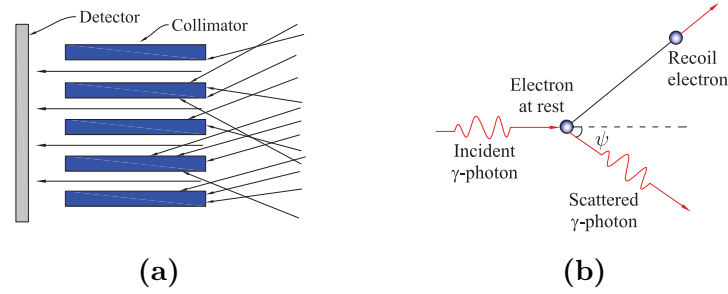

Figure 1: Principles of mechanical collimation (a) and Compton scattering (b).

A Compton camera consists of two parallel position and energy sensitive detectors (see Fig. 2(a)). When the incoming gamma photon hits the camera, it undergoes Compton scattering in the first detector (scatterer) and photoelectric absorption in the second detector (absorber). In both interactions, the positions u and v and the energies E_1 and E_2 of the photon are recorded. The scattering angle ψ and a unit vector β are calculated from the data as follows (see e.g. [11]):

$$\cos \psi = 1 - \frac{mc^2 E_1}{(E_1 + E_2)E_2} \qquad \beta = \frac{u - v}{|u - v|}. \tag{1}$$

Here, m is the mass of the electron and c is the speed of light.
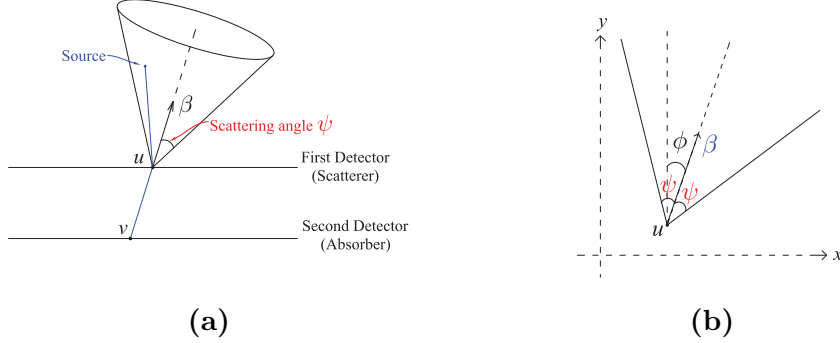
Figure 2: Schematic represantation of a Compton camera (a) and a cone in 2D (b).

From the knowledge of the scattering angle ψ and the vector β, we can conclude that the photon originated from the surface of the cone with central axis β, vertex u and opening angle ψ (see Fig. 2(a)). Therefore, although the exact incoming direction of the detected particle is not available, one knows a surface cone of possible directions. One can argue that the data provided by Compton camera are integrals of the distribution of the radiation sources over conical surfaces having vertex at the detector. The operator that maps source intensity distribution function $f(x)$ to its integrals over these cones is called the *cone* or *Compton transform*. The goal of Compton camera imaging is to recover source distribution from this data [1].

In the Compton camera imaging applications mentioned above, the vertex of the cone is located on the detector array, while in some other applications the vertices are not restricted, although some other conditions are imposed on the cones. Also, in the Compton case, the data from all cones emanating from a given detector position is collected, while in some other applications only some cones (e.g., those with a prescribed axial direction) with a given vertex are involved. Having the Compton imaging in kind, we thus follow the started in [37] line of studying analytic and numerical properties of the general cone transform, where all cones with a given vertex are accounted for, with the hope of obtaining consequences for more restricted version arising in practice (e.g., in Compton camera imaging). This partially materialized in [37] in the much simpler $2D$ case. Here we address the n-dimensional situation (with main emphasis on $n = 3$) and implement numerically some

inversion formulas from [37], as well as some new ones developed below. In particular, we address a realistic situation arising in the Compton camera imaging.

The problem of inverting the cone transform is over-determined (the space of 3D cones with vertices on a detector surface is five-dimensional, three-dimensional in 2D). Without the restriction on the vertex, the dimensions are correspondingly six and four. One thus could restrict the set of cones, in order to get a non-over-determined problem (e.g. [3, 4, 6, 8, 16, 17, 19–21, 26, 29, 34, 38, and references therein]). In most of these considerations only a subset of cones with vertex at a given detector is used. This means that most of the information already collected by this Compton camera is discarded. However, when the signals are weak (e.g. in homeland security applications [1]), restricting the data would lead to essential elimination of the signal. We thus intend to use the data coming from all cones converging to each detector. We also discuss viable restrictions on detector arrays.

In order to avoid being distracted from the main purpose of this text, we make in all theorems a severe overkill assumption that the functions in question belong to the Schwartz space $\mathcal{S}$ of smooth fast decaying functions. This allows us skip discussions of applicability of various transforms. However, as it is in the case of Radon transform (see, e.g. [28, 31]), the results have a much wider area of applicability, as in particular our numerical implementations show. The issues of appropriate functional spaces will be addressed elsewhere.

The paper is organized as follows. In the next section 1, we recall briefly some relevant transforms and their properties. In section 2, we obtain several procedures that convert the cone data to the Radon data of the same function. Section 3 contains the results of numerical implementation of these approaches in $3D$. Remarks and conclusions can be found in section 4. The last section contains acknowledgments.

1 Definitions

A round surface cone in $\mathbb{R}^n$ can be parametrized by a tuple (u, β, ψ), where $u \in \mathbb{R}^n$ is the cone's vertex, the unit vector $\beta \in S^{n-1}$ is directed along the cone's central axis, and the opening angle is $\psi \in (0, \pi)$ (see Fig. 2(a)). A point $x \in \mathbb{R}^n$ lies on the cone iff

$$(x - u) \cdot \beta = |x - u| \cos \psi. \tag{2}$$

4

The *cone transform* C maps a function f to its integrals over all circular cones in $\mathbb{R}^n$:

$$Cf(u, \beta, \psi) = \int_{(x-u)\cdot\beta=|x-u|\cos\psi} f(x)dx, \qquad (3)$$

where dx is the surface measure on the cone.

In two dimensions, the equation (2) describes two rays with a common vertex (see Fig. 2(b)), which are also called as V-lines or broken lines in the literature. Then, the 2D cone transform of a function is its integral over these V-lines. That is, for $\beta = \beta(\phi) = (\sin\phi, \cos\phi) \in S^1$, the 2D cone transform of a function $f \in \mathcal{S}(\mathbb{R}^2)$ is given by

$$Cf(u, \beta(\phi), \psi)$$
$$= \int_0^\infty [f(u + r(\sin(\psi + \phi), \cos(\psi + \phi))) + f(u + r(-\sin(\psi - \phi), \cos(\psi - \phi)))]dr.$$
$$(4)$$

We also recall that the n-dimensional *Radon transform* R maps a function f on $\mathbb{R}^n$ into the set of its integrals over the hyperplanes in $\mathbb{R}^n$. Namely, if $\omega \in S^{n-1}$ and $s \in \mathbb{R}$,

$$Rf(\omega, s) = \int_{x\cdot\omega=s} f(x)dx. \qquad (5)$$

In this setting, the Radon transform of f is the integral of f over the hyperplane orthogonal to ω at the signed distance s from the origin.

The following inversion formula is well known (e.g., [28]):

$$f = \frac{1}{2}(2\pi)^{1-n}I^{-\alpha}R^{\#}I^{\alpha-n+1}Rf, \qquad \alpha < n. \qquad (6)$$

Here, $R^{\#}$ is the *backprojection operator* [28] and I^{α}, $\alpha < n$, is the *Riesz potential* acting on a function f as

$$\widehat{(I^{\alpha}f)}(\xi) = |\xi|^{-\alpha}\hat{f}(\xi),$$

where $\hat{f}$ is the Fourier transform of f (see e.g. [18, 22, 28]).

The *cosine transform* of a function $f \in C(S^{n-1})$ is defined by

$$\mathfrak{C}f(\omega) = \frac{1}{|S^{n-1}|}\int_{S^{n-1}} f(\sigma)|\sigma \cdot \omega|d\sigma, \qquad (7)$$

for all $\omega \in S^{n-1}$ (see e.g. [13, 31]).

We will also need to use the *Funk transform* (e.g., [14, 18, 30, 31]) that integrates a function on the sphere over all great circles (hyperplane sections). Several inversion formulas for the Funk transform exist in the literature [9, 10, 14, 18, 30, 31].

2 Various inversion formulas for the cone transform

We start with a basic relationship between the cone, Radon and cosine transforms:

Theorem 1 ([37]). *Let $f \in \mathcal{S}(\mathbb{R}^n)$ and T_a be the translation operator in $\mathbb{R}^n$, defined as $T_a f(x) = f(x + a)$ for $a \in \mathbb{R}^n$. Then, for any $u \in \mathbb{R}^n$ and $\beta \in S^{n-1}$, we have*

$$\int_0^\pi Cf(u, \beta, \psi) \sin(\psi) d\psi = \frac{\pi}{|S^{n-1}|} \int_{S^{n-1}} Rf(\omega, u \cdot \omega) |\omega \cdot \beta| d\omega = \mathfrak{C}(R(T_u f))(\beta),$$

(8)

where $|S^{n-1}|$ denotes the area of the sphere S^{n-1}.

The proof of this relation can be found in [37].

Since the cosine transform is a continuous automorphism of $C_{even}^\infty(S^{n-1})$ (see e.g. [13, 31]), and for any $f \in \mathcal{S}(\mathbb{R}^n)$, $Rf(\omega, 0)$ is an even function in $C^\infty(S^{n-1})$, we can recover the function $R(T_u f)$ by inverting the cosine transform. Using the inversion formula for the cosine transform given in [31, Chapter 5, Theorem 5.35], we obtain the formulas given in Theorem 2 below that recover the Radon data from the cone data. Then, inverting the Radon transform [28], one recovers the function f.

Theorem 2 ([37]). *Let $f \in \mathcal{S}(\mathbb{R}^n)$. For any $u \in \mathbb{R}^n$ and $\omega \in S^{n-1}$,*

(i) if n is odd,

$$Rf(\omega, \omega \cdot u) = \frac{\Gamma(\frac{n+1}{2})}{2\pi^{(n+1)/2}} \int_{S^{n-1}} \int_0^\pi Cf(u, \beta, \psi) \sin \psi d\psi d\beta$$

$$- \frac{2\pi^{-n/2}}{\Gamma(\frac{n}{2})} P_{(n+1)/2}(\Delta_S) \left\{ \int_{S^{n-1}} \int_0^\pi Cf(u, \beta, \psi) \log \frac{1}{|\omega \cdot \beta|} \sin \psi d\psi d\beta \right\},$$

$$(9)$$

(ii) if n is even,

$$Rf(\omega, \omega \cdot u) = \frac{-2^{n-1}}{\Gamma(n-1)} \int_0^\pi P_{n/2}(\Delta_S) F(Cf)(u, \omega, \psi) \sin \psi d\psi, \quad (10)$$

where F is the Funk transform, Δ_S is the Laplace-Beltrami operator on S^{n-1} acting on ω, and

$$P_r(\Delta_S) = 4^{-r} \prod_{k=0}^{r-1} \left[-\Delta_S + (2k-1)(n-1-2k) \right].$$

This result, in particular, answers the question of what geometries of Compton detectors are sufficient for (stable) reconstruction of the function f. Indeed, formulas (9) and (10) show that it is sufficient to have for any $\omega \in S^{n-1}$ and $s \in \mathbb{R}$ a detector location u such that $\omega \cdot u = s$. This can be rephrased in a nice geometric way:

Definition 3 (*Compton Admissibility Condition*)**.** We will call an array of Compton detectors *admissible* (for a given region of space), if any hyperplane intersecting this region, intersects a detector.

So, if a set U of detectors is admissible for a region $D \in \mathbb{R}^n$, then the formulas (9) and (10) enable one to reconstruct the Radon transform of any function f supported inside D, and thus f itself.

Here is an useful example of an application of the admissibility:

Proposition 4. *Suppose that $n = 3$ and the detectors are placed on a sphere S_r of radius r. We assume that the region for placing the object to be imaged is the concentric sphere $S_{r'}$ of radius $r' = r - \delta$ for some $\delta > 0$. Then, any curve U on S_r that satisfies the condition below is admissible:*

Any circle on S_r of radius $\rho \geq \sqrt{\delta(2r - \delta)}$ intersects U.

Proof. Indeed, every plane intersecting the interior of the sphere $S_{r'}$ intersect S_r over a circle of radius $\rho \geq \sqrt{\delta(2r - \delta)}$ and thus contains at least one detector. $\qquad\square$

Remark 5.

(i) The experience of Radon transform shows that uniqueness of reconstruction should hold for some non-admissible sets of detectors as well, although some ("invisible") sharp details will get blurred in the reconstruction (see, e.g. [22]). The corresponding microlocal analysis of this issue will be done elsewhere.

(ii) The admissibility condition is not the minimal one. For instance, in the situation of Proposition 4, the set of Compton data will still be 4-dimensional, and thus somewhat overdetermined. To avoid overdetermined data, one could use a single detector, which would lead to some sharp features of the image being blurred.

(iii) In the cases of low signal-to-noise ratio (e.g. SPECT and especially homeland security imaging), one would prefer to use larger admissible sets of detectors (e.g. 2D rather than 1D arrays considered in Proposition 4), which would allow introducing additional (weighted) averaging, in order to reduce the effects of the noise.

A different approach to recovery of the Radon data from the Compton data comes from the following known relation (see [15]) between the cosine and Funk transforms:

$$(\Delta_S + n - 1)\mathfrak{C} = F, \tag{11}$$

where Δ_S is the Laplace-Beltrami operator on the sphere.

Indeed, applying $(\Delta_S + n - 1)$ to (8), we obtain

$$\Phi(u, \beta) := F(R(T_u f))(\beta) = \frac{(\Delta_S + n - 1)}{\pi} \int_0^\pi Cf(u, \beta, \psi) \sin \psi \, d\psi, \tag{12}$$

where Δ_S acts in variable β.

We now use the inversion formula for the Funk transform given in [31, Chapter 5, Theorem 5.37], whose application to (12) leads to the following result.

Theorem 6. *Let* $f \in \mathcal{S}(\mathbb{R}^n)$. *For any* $u \in \mathbb{R}^n$ *and* $\omega \in S^{n-1}$,

$$Rf(\omega, \omega \cdot u) = \frac{2^{n-1}}{(n-2)!} Q(\Delta_S) \left\{ \int_{S^{n-1}} \Phi(u, \beta) \log \frac{1}{|\omega \cdot \beta|} d\beta \right\}$$
$$+ \frac{\Gamma(n/2)}{2\pi^{n/2}} \int_{S^{n-1}} \Phi(u, \beta) d\beta, \tag{13}$$

where $Q(\Delta_S) = 4^{(1-n)/2} \prod_{k=0}^{(n-3)/2} [-\Delta_S + (2k+1)(n-3-2k)]$.

In particulary, in $3D$ one arrives to

Corollary 7. *For any* $u \in \mathbb{R}^3$ *and* $\omega \in S^2$,

$$Rf(\omega, \omega \cdot u) = \frac{-\Delta_S}{2\pi} \left\{ \int_{S^{n-1}} \Phi(u, \beta) \log \frac{1}{|\omega \cdot \beta|} d\beta \right\}$$
$$+ \frac{1}{4\pi} \int_{S^{n-1}} \Phi(u, \beta) d\beta. \tag{14}$$

3   Reconstructions in 3D

Some numerical results in 2-dimensions were presented in [37]. Here, we address the much more complicated 3-dimensional case, where we develop and apply three different inversion algorithms and study their feasibility.

Our first attempt has been to implement numerically the inversion formula (9) from Theorem 2. The results were discouraging. The reason for this failure was that (9) requires numerical computation of some singular integrals, followed then by applying to the results a fourth order differential operator on the sphere.

Thus we had to resort to different inversion techniques, the description of which one finds below.

In all examples below, the detectors cover the unit sphere $\mathbb{S}^2$ in $\mathbb{R}^3$ and the object is located inside and at some positive distance from this sphere. The forward simulations of Compton camera data were done numerically rather than analytically and thus involved errors, which is better for checking the validity and stability of the reconstruction algorithms.

3.1 Method 1: Reconstruction using spherical harmonics expansions

Let us introduce the function

$$G(u, \beta) := \int_0^\pi Cf(u, \beta, \psi) \sin \psi d\psi.$$

For each fixed detector location $u \in \mathbb{R}^n$, we can expand the function $G(u, \beta)$ of $\beta \in S^{n-1}$ into spherical harmonics Y_l^m:

$$G(u, \beta) = \sum_{l=0}^\infty \sum_{m=1}^{N(n,l)} g_l^m(u) Y_l^m(\beta), \qquad (15)$$

where

$$g_l^m(u) = \int_{S^{n-1}} G(u, \beta) \overline{Y_l^m(\beta)} d\beta$$

and

$$N(n, l) = (n + 2l - 2) \frac{(n + l - 3)!}{l!(n - 2)!}$$

(see e.g. [5, 27, 35]). Using (9), one obtains the following series inversion formula:

Theorem 8. *For any $u \in \mathbb{R}^n$ and $\omega \in S^{n-1}$,*

$$Rf(\omega, \omega \cdot u) = \frac{\Gamma(\frac{n+1}{2})}{\pi^{n/2}} g_0^1(u) - \frac{2\pi^{-n/2}}{\Gamma(\frac{n}{2})} \sum_{l=1}^\infty d_l q_{n,l} \sum_{m=1}^{N(n,l)} g_l^m(u) Y_l^m(\omega), \qquad (16)$$

where

$$q_{n,l} = 4^{-(n+1)/2} \prod_{k=0}^{(n-1)/2} [l(l + n - 2) + (2k - 1)(n - 1 - 2k)] \qquad (17)$$

and

$$d_l = |S^{n-2}| \int_{-1}^1 \log \frac{1}{|t|} L_l(t)(1 - t^2)^{(n-3)/2} dt, \qquad (18)$$

with L_l being the l-th degree Legendre polynomial (see e.g. [36]).

10

Proof. Plugging (15) into the second term in the right hand side of (9), we obtain

$$Rf(\omega, \omega \cdot u) = \frac{\Gamma(\frac{n+1}{2})}{2\pi^{(n+1)/2}} \int\limits_{S^{n-1}} G(u, \beta) d\beta$$

$$- \frac{2P_{(n+1)/2}(\Delta_S)}{\pi^{n/2}\Gamma(\frac{n}{2})} \sum_{l=0}^{\infty} \sum_{m=1}^{N(n,l)} g_l^m(u) \int\limits_{S^{n-1}} \log \frac{1}{|\omega \cdot \beta|} Y_l^m(\beta) d\beta. \tag{19}$$

We note that $\int\limits_{S^{n-1}} G(u, \beta) d\beta = 2\sqrt{\pi} g_0^1(u)$. Then Funk-Hecke formula (see e.g. [27]) implies that

$$\int\limits_{S^{n-1}} \log \frac{1}{|\omega \cdot \beta|} Y_l^m(\beta) d\beta = d_l Y_l^m(\omega),$$

where d_l is as in (18). Also, since $\Delta_S Y_l = -l(l+n-2)Y_l$, $l = 0, 1, 2, ...$, we have $P_{(n+1)/2}(\Delta_S) Y_l = q_{n,l} Y_l$, where $q_{n,l}$ is given in (17). Hence, we get the result. $\square$

In particular, for $n = 3$, we get

Corollary 9. *For any $u \in \mathbb{R}^3$ and $\omega \in S^2$,*

$$Rf(\omega, \omega \cdot u) = \pi^{-3/2} g_0^1(u) - \frac{1}{4\pi^2} \sum_{l=1}^{\infty} d_l q_l \sum_{m=1}^{2l+1} g_l^m(u) Y_l^m(\omega), \tag{20}$$

where $q_l = (l-1)l(l+1)(l+2)$ and $d_l = 2\pi \int\limits_{-1}^{1} \log \frac{1}{|t|} L_l(t) dt$ with L_l being the l-th degree Legendre polynomial.

In our numerical tests, the phantom was the characteristic function of the $3D$ ball of radius 0.5 centered at the origin. The reason for considering a radial phantom is that its Radon transform can easily be computed analytically. On the other hand, the Compton data was simulated numerically and then used to numerically reconstruct the Radon data. The results can then be compared with the exact (analytically computed) Radon transforms[1].

---

[1]Tests on non-radial phantoms have lead to the similar results.

Figure 3 shows the comparison of the analytically computed Radon transform of the phantom (shown in red) with its reconstructions, using (20), for varying discretization of the sphere. The number of terms considered in the expansion (15) is shown at the top of each figure as L. In order to reduce the effect of instability, we have taken less terms in the computation of the Radon transform via (20). These are shown as Lt in the figures.
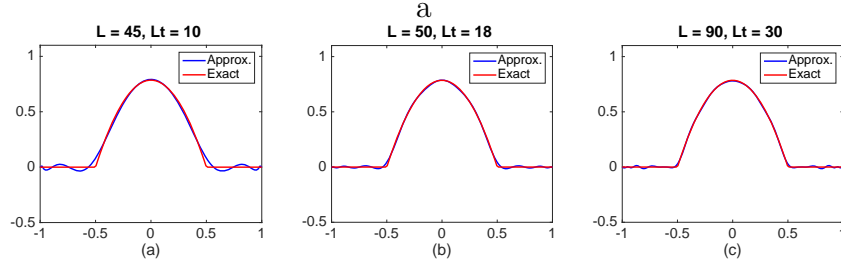
Figure 3: The analytically computed Radon transform of the phantom (shown in red) vs. its reconstruction from the Compton data using (20). The reconstructions shown correspond to three different mesh sizes: the number of points on the sphere being 1806, 7446, and 30000, from left to right.

3.2 Method 2: Reconstruction by direct implementation of Theorem 6

As we have mentioned before, the direct numerical implementation of the formula (9) in 3D required the application of the fourth order differential operator $\Delta_S(\Delta_S+2)$ on the sphere to the result of numerical implementation of a singular integral. The authors could not make it work well. The advantage of using (14) is that one needs to apply two second order operators acting in different variables and with a smoothing operator sandwiched in between. This makes such a calculation feasible.

In our numerical implementations, we used the algorithm for the discrete Laplace-Beltrami operator given in [7]. It is based on the heat equation used to create a point-wise convergent approximation for the Laplace-Beltami operator on a surface. For a function f given at the set V of vertices of a

mesh K on the 2-sphere, it is computed, for any $v \in V$, as follows:

$$\Delta_K^h f(v) = \frac{1}{4\pi h^2} \sum_{t \in K} \frac{Area(t)}{\#t} \sum_{p \in V(t)} e^{-\frac{\|p-v\|^2}{4h}} (f(p) - f(v)). \qquad (21)$$

Here, for any face $t \in K$, the number of vertices in t is denoted by $\#t$, and $V(t)$ is the set of vertices of t. The parameter h is a positive quantity (akin to the time in the heat equation), which intuitively corresponds to the size of the neighborhood considered at each point. The authors of [7] suggest that h can be taken to be a function of v, which allows the algorithm to adapt to the local mesh size.

In our experiments, we used the adaptive parameter $h(v) = 0.125 \times$ (the average edge length at v). We used the same phantom as in the previous section. Figure 4 shows the reconstructions of the Radon transform of the phantom for varying discretization of the sphere.
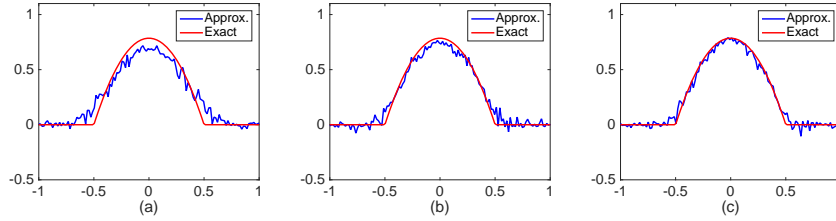
Figure 4: The Radon transform of the phantom recovered using (14) and (21). The reconstructions shown corresponds to three different mesh sizes: the number of points on the sphere being 1806, 7446, and 30000, from left to right.

These results do not seem to indicate presence of any systemic error and thus suggest that a touch of smoothing could lead to a significant improvement. This indeed happens to be the case, as Figure 5 shows.
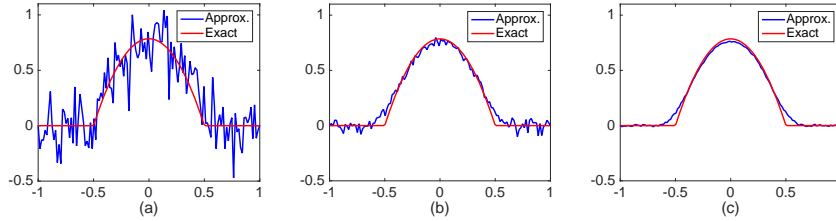
13
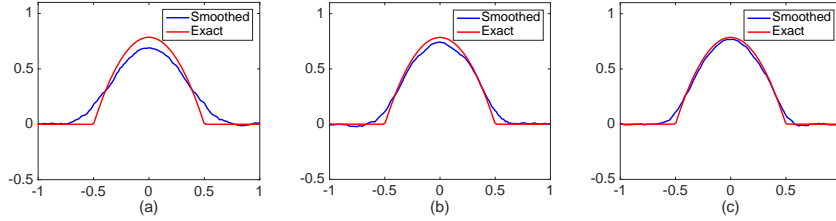
Figure 5: The Radon transforms shown in Figure 4 are smoothed by a moving average filter having span 9. The reconstructions shown corresponds to three different mesh sizes: the number of points on the sphere being 1806, 7446, and 30000, from left to right.

3.3 Method 3: Reconstruction via approximate inversion of the Cosine Transform

The formula (8) shows that availability of any cosine transform inversion would also lead to an inversion of the cone transform, and such approximate and exact inversions indeed exist [25, 31, 32]. We apply here the method of approximate inverse developed in [24, 25, 32], which is an incarnation of a general approach to solving inverse problems numerically. Namely, for a given data h, the aim is to find g satisfying $\mathfrak{C}g = h$. If we find a 'Green's function' ψ such that $\mathfrak{C}\psi = \delta$, then the spherical convolution $h * \psi$ of h and ψ solves the equation $\mathfrak{C}g = h$. Now, if one picks a 'mollifier' (an approximation to the δ-function) δ_γ and "approximate Greens function" ψ_γ, such that $\mathfrak{C}\psi_\gamma = \delta_\gamma$, then one finds the approximate solution $g_\gamma = g * \psi_\gamma$.

In our numerical tests, we used the reconstruction kernel ψ_γ that was analytically computed in [32] for a special class of mollifiers (see [32, (4.1) and (4.10)]). We used the same phantom as in the previous sections. Figure 6 shows the reconstructions of the Radon transform of the phantom for varying discretization of the sphere.

14

Figure 6: The Radon transform of the phantom using the method of approximate inverse for the cosine transform. The reconstructions shown corresponds to three different mesh sizes: the number of points on the sphere being 1806, 7446, and 30000, from left to right.

One notices insufficient resolution of singularity which is due to the insufficiently fine approximation of δ-function by δ_γ chosen in [24, 25, 32].

3.4 Comparison of the three methods

While above we only addressed reconstructing the Radon transform of the function in question, here we show how the three methods perform after taking the final step of inverting the Radon transform and reconstructing the characteristic function of the ball.

Figure 7 shows the three cross-sections of the spherical phantom and of its reconstructions from the Radon data obtained via the three methods above. The finest mesh on the sphere (30000 points) was used.
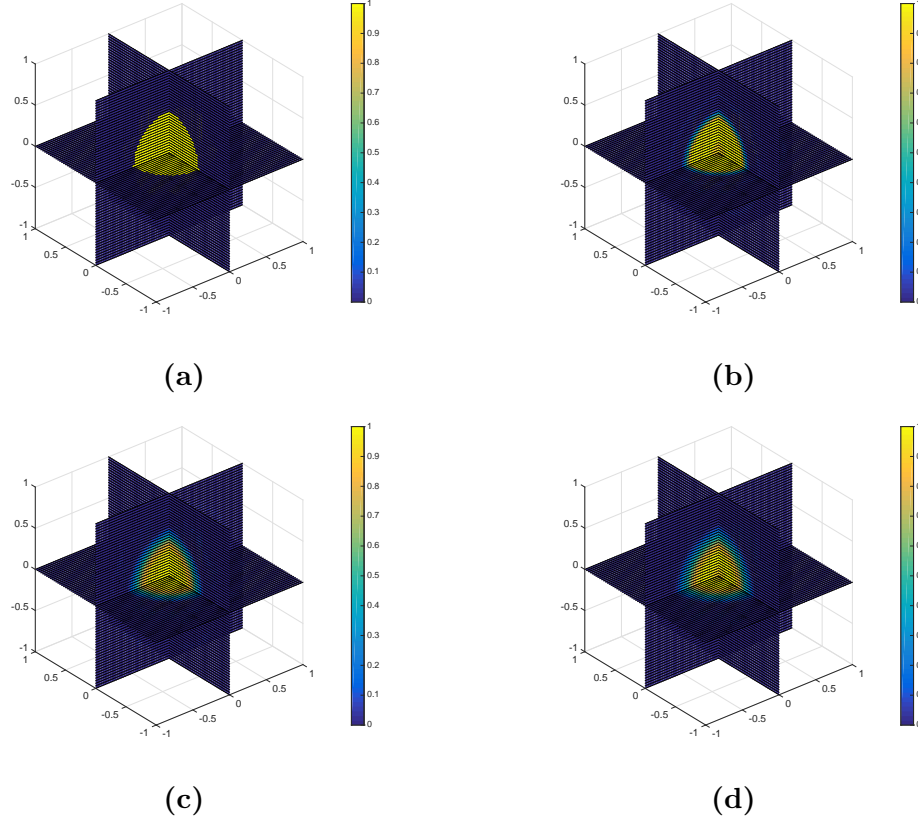
Figure 7: Comparison of the three reconstruction methods. The cross-sections by the coordinate planes are shown. (a) The phantom is the characteristic function of 3d ball having radius 0.5 and center at the origin. (b) Reconstruction via Method 1. (c) Reconstruction via Method 2. (d) Reconstruction via Method 3.

The L^∞ errors between the approximate and exact Radon transforms for Methods 1, 2 and 3 were 2.65%, 14.18% and 15.01%, respectively. There was no significant difference between the three methods in terms of computation time. Thus, overall our current results indicate that overall the Method 1 outperforms the other two.

It is important to note that in all of the methods, there are parameters that can still be optimized, namely L and Lt in Method 1, h in Method 2, and γ in Method 3 (see [32]).

4 Conclusion and Remarks

(i) Several new analytical techniques are developed and successfully numerically implemented for inverting the Compton camera data. A comparison of these methods is provided.

(ii) Although the algorithms surely could benefit from further improvement, the feasibility of the approach has been shown.

(iii) It is argued that in the case of Compton camera imaging, reducing the set of cones "visible" from a detector (e.g., considering only the cones with a given axial direction), which was done in most previous studies, seems to be a not very good idea (especially in presence of low SNR), since this amounts to discarding the already collected data, which can be used for stabilizing the reconstruction.

(iv) A general "admissibility" criterion for the set of detectors is formulated. Under this condition, the formulas provided allow reconstructions for an otherwise arbitrary geometry of detector arrays.

Acknowledgements

References

[1] Allmaras M, Darrow D P, Hristova Y, Kanschat G and Kuchment P 2013 Detecting small low emission radiating sources *Inverse Problems Imaging* **7** 47-79

[2] Allmaras M, Charlton W, Ciabatti A, Hristova Y, Kuchment P, Olson A, and Ragusa J 2016 Detecting small low emission sources - case studies, preprint arXiv:1309.5974, to appear in Nuclear Sci. and Eng.

[3] Ambartsoumian G. 2012 Inversion of the V-line Radon transform in a disc and its applications in imaging, Computers & Mathematics with Applications. Mathematical Methods and Models in Biosciences , Volume 64, Issue 3, Pages 260265

[4] Ambartsoumian G. and Moon S. 2013 Computers & Mathematics with Applications. BioMath 2012 Volume 66, Issue 9, Pages 15671572

[5] Axler S, Bourdon P, and Ramey W, 2001 *Harmonic function theory.*Graduate Texts in Mathematics, 137. Springer-Verlag, New York.

[6] Basko R, Zeng G L and Gullberg G T 1998 Application of spherical harmonics to image reconstruction for the Compton camera *Phys. Med. Biol.* **43** 887-894

[7] Belkin M, Sun J, and Wang Y 2008 Discrete Laplace operator on meshed surfaces *In Symposium on Computational Geometry* 278-287.

[8] Cree M J and Bones P J 1994 Towards direct reconstruction from a gamma camera based on Compton scattering *IEEE Trans. Med. Imaging* **13** 398-409

[9] Funk P 1913 Über Flächen mit lauter geschlossenen geodätischen Linien *Mathematische Annalen* **74**(2) 278-300

[10] Funk P 1916 Über eine geometrische Anwendung der Abelschen Integralgleichung *Mathematische Annalen* **77** 129-135

[11] Everett D B, Fleming J S, Todd R W and Nightingale J M 1977 Gamma-radiation Imaging System Based on the Compton Effect *Proc. IEE* **124** 995-1000

[12] Florescu L, Markel V A and Schotland J C 2011 Inversion formulas for the broken-ray Radon transform *Inverse Problems* **27** 025002

[13] Gardner R J 2006 *Geometric Tomography* (Encyclopedia of Mathematics and its Applications) (New York: Cambridge University Press)

[14] Gelfand I, Gindikin S, and Graev M 2003 *Selected Topics in Integral Geometry.* Transl. Math. Monogr. v. 220, Amer. Math. Soc., Providence RI.

[15] Goodey P and Weil W 1992 Centrally Symmetric Convex Bodies and the Spherical Radon Transform *J. Differential Geometry* **35** 675-688

[16] Gouia-Zarrad R and Ambartsoumian G 2014 Exact inversion of the conical Radon transform with a fixed opening angle *Inverse Problems* **30** 045007

[17] Haltmeier M 2014 Exact Reconstruction Formulas for a Radon Transform over Cones *Inverse Problems* **30** 035001

[18] Helgason S 2011 *Integral Geometry and Radon Transforms* (Berlin: Springer)

[19] Hristova Y 2010 Mathematical problems of thermoacoustic and Compton camera imaging Dissertation Texas A&M University.

[20] Hristova Y 2015 Inversion of a V-line transform arising in emission tomography. Journal of Coupled Systems and Multiscale Dynamics, **3**, Number 3, pp. 272-277.

[21] Jubg C.-Y. and Moon S. 2015 Inversion formulas for cone transforms arising in application of Compton cameras. Inverse Problems, **31**, Number 1, 015006.

[22] Kuchment P 2014 *The Radon Transform and Medical Imaging* (Philadelphia: Society for Industrial and Applied Mathematics)

[23] Kishimoto A, Kataoka J, Nishiyama T, Taya T and Kabuki S 2015 Demonstration of three-dimensional imaging based on handheld Compton camera *Journal of Instrumentation* **11** 11001

[24] Louis A K and Maass P 1990 A mollifier method for linear operator equations of the first kind *Inverse Problems* **6** 427-40

[25] Louis A K, Riplinger M, Spiess M and Spodarev E 2011 Inversion algorithms for the spherical Radon and cosine transform *Inverse Problems* **27** 035015

[26] Moon S 2015 On the determination of a function from its cone transform with fixed central axis arXiv:1503.07616

[27] Muller C 1966 *Spherical Harmonics* (Lecture Notes in Mathematics 17) (Berlin: Springer)

[28] Natterer F 2001 *The Mathematics of Computerized Tomography* (Classics in Applied Mathematics) (Philadelphia: Society for Industrial and Applied Mathematics)

[29] Nguyen M K, Truong T T and Grangeat P 2005 Radon transforms on a class of cones with fixed axis direction *J. Phys. A: Math. Gen.* **38** 8003-8015

[30] Palamodov V. 2004 *Reconstructive Integral Geometry*, Birkhäuser, Basel.

[31] Rubin B 2015 *Introduction to Radon Transforms: With Elements of Fractional Calculus and Harmonic Analysis* (Encyclopedia of Mathematics and its Applications) (New York: Cambridge University Press)

[32] Riplinger M and Spiess M 2014 Numerical inversion of the spherical Radon transform and the cosine transform using the approximate inverse with a special class of locally supported mollifiers *J. Inverse Ill-Posed Probl.* **22** 497-536

[33] Singh M 1983 An electronically collimated gamma camera for single photon emission computed tomography: I. Theoretical considerations and design criteria Med. Phys. **10** 421427

[34] Smith B 2005 Reconstruction methods and completeness conditions for two Compton data models J. Opt. Soc. Am. A **22** 445459.

[35] Stein, Elias M, Weiss, Guido 1971 *Introduction to Fourier analysis on Euclidean spaces.* Princeton Mathematical Series, No. 32. Princeton University Press, Princeton, N.J.

[36] Szego G 1939 *Orthogonal Polynomials* (Colloquium Publications) (New York: American Mathematical Society)

[37] Terzioglu F 2015 Some Inversion Formulas for the Cone Transform *Inverse Problems* **31** 115010

[38] Truong, T and Nguyen, M 2015 New properties of the V-line Radon transform and their imaging applications. J. Phys. A **48** no. 40, 405204, 28 pp.

[39] Xun X, Mallick B, Carroll R, and Kuchment P 2011 Bayesian approach to detection of small low emission sources, Inverse Problems **27** 115009.